Structure and stability of isotropic states of hard platelet fluids

David L. Cheung,[1,*] Lucian Anton,[2,3,†] Michael P. Allen,[1,‡] Andrew J. Masters,[2,§] Jonathan Phillips,[4] and Matthias Schmidt[4,5]
[1]*Department of Physics and Centre for Scientific Computing, University of Warwick, Coventry, CV4 7AL, United Kingdom*
[2]*School of Chemical Engineering and Analytical Science, University of Manchester, Sackville Street, Manchester, M60 1QD, United Kingdom*
[3]*Institute of Atomic Physics, INFLPR, Lab 22, PO Box MG-36 R76900, Bucharest, Romania*
[4]*H H Wills Physics Laboratory, University of Bristol, Royal Fort, Tyndall Avenue, Bristol BS8 1TL, United Kingdom*
[5]*Theoretische Physik II, Universität Bayreuth, Universitätsstraße 30, D-95440 Bayreuth, Germany*
(Received 6 August 2008; published 7 October 2008)

We study the thermodynamics and the pair structure of hard, infinitely thin, circular platelets in the isotropic phase. Monte Carlo simulation results indicate a rich spatial structure of the spherical expansion components of the direct correlation function, including nonmonotonical variation of some of the components with density. Integral equation theory is shown to reproduce the main features observed in simulations. The hypernetted chain closure, as well as its extended versions that include the bridge function up to second and third order in density, perform better than both the Percus-Yevick closure and Verlet bridge function approximation. Using a recent fundamental measure density functional theory, an analytic expression for the direct correlation function is obtained as the sum of the Mayer bond and a term proportional to the density and the intersection length of two platelets. This is shown to give a reasonable estimate of the structure found in simulations, but to fail to capture the nonmonotonic variation with density. We also carry out a density functional stability analysis of the isotropic phase with respect to nematic ordering and show that the limiting density is consistent with that where the Kerr coefficient vanishes. As a reference system, we compare to simulation results for hard oblate spheroids with small, but nonzero elongations, demonstrating that the case of vanishingly thin platelets is approached smoothly.

DOI: 10.1103/PhysRevE.78.041201 PACS number(s): 61.20.Gy, 61.20.Ja, 05.20.Jj

I. INTRODUCTION

Knowledge of the microscopic structure of classical fluids provides valuable insights into their macroscopic properties and behavior [1,2]. Both theory and simulation have been successfully used to study simple fluids, which are characterized by spherically symmetric pair interaction potentials and to model a wide range of substances from noble gases to colloidal dispersions. Integral equation theories (IETs), using approximations such as the hypernetted chain (HNC) or Percus-Yevick (PY) closure relations, are capable of making very accurate predictions for the structural correlations on the pair level and, as a consequence, for the thermodynamics of such systems. More advanced closure relations can be based on hybrid versions of the above closures that are enforced to be thermodynamically consistent [3] or on the incorporation of approximate bridge functions into the HNC closure [4], or on the inhomogeneous Ornstein-Zernike equation [5].

The equilibrium properties of systems of nonspherical particles are, as compared to the case of simple fluids, less well understood. In such systems the pair interaction potential depends not only on the center-to-center distance of the particles but also on their orientations. Simple versions of such systems include axially symmetric particles where IET has been used successfully to study models such as hard spheroids [6], spherocylinders [7], and hard cut spheres [8]. These studies suggest that results from the HNC closure are in general superior to those from the PY approximation. However, serious discrepancies between theory and simulation results remain, in particular at high densities [6,9–11]. Significant attempts have been made to improve the performance of IET for molecular fluids [12–17]. However, the theoretical work has been hampered by the paucity of simulation data for such systems. Until recently there were only few simulation studies aimed at obtaining the direct correlation function of molecular fluids [18,19] and only a single calculation of the bridge function (for hard diatomic molecules) was available [20].

In recent work, some of us have used Monte Carlo (MC) simulations and integral equation theory (IET) to study the pair structure of model molecular fluids consisting of axially symmetric spheroids; such particles are characterized by the length A of the symmetry axis, and the length D of the two degenerate perpendicular axes; moderately prolate ($1 \leqslant A/D \leqslant 5$) and oblate ($0.2 \leqslant A/D \leqslant 1$) spheroids as well as their mixtures were studied [21–23]. In the current paper, this work is extended to fluids of hard, infinitely thin platelets [24–26]; these are formally obtained in the limit $A/D \to 0$. We also investigate highly oblate spheroids with a nonzero aspect ratio ($0.01 \leqslant A/D \leqslant 0.1$) as a reference case in order to assess the robustness of the former model.

Besides providing a stringent test case for both theory and simulation techniques, studying the model is motivated by discotic molecules, which have important applications due to

*Present address: Department of Chemistry, University of Warwick, Coventry, CV4 7AL, UK. david.cheung@warwick.ac.uk
†Present address: NAG Ltd, Barnett House, 53 Fountain Street, Manchester M2 2AN, UK. lucian.anton@nag.co.uk
‡m.p.allen@warwick.ac.uk
§andrew.masters@manchester.ac.uk

their liquid crystalline properties [27–29]. Further interest in discotic models comes from dispersions of colloidal platelets which have been shown to display a wealth of interesting physical phenomena [30–35]. Recent work was aimed at elucidating interfacial behavior at substrates and interfaces between coexisting isotropic and nematic bulk phases [36], using the hard platelet fluid as a minimal model for such complex liquids. There is vital interest in the behavior of liquid crystals in confined geometry [37–41], and density functional theory [42] constitutes a powerful tool for investigation. In contrast to the celebrated case of thin hard rods, Onsager theory [43] is known to perform poorly for platelets. Although it does predict a first order isotropic-nematic phase transition, the coexistence densities and density jump are significantly overestimated.

Based on earlier work [44] a fundamental measure theory (FMT) density functional was constructed [45] and used to study the properties of inhomogeneous hard platelet fluids, such as wetting of a hard wall by the nematic phase when the bulk is isotropic and bulk isotropic-nematic coexistence is approached [36,46,47]. These interfacial studies depend crucially on a satisfactory description of the bulk phases involved, and indeed it was shown [36,46,47] that the coexistence densities and the equation of state agree reasonably well with simulation results. In the present work we investigate in more detail the pair structural correlations in the isotropic phase.

The paper is organized as follows. In Sec. II an overview of the closure relations used in the IET and technical details about the expansion in spherical harmonics and numerical implementation is given. Section III gives details about the simulation methods. Section IV gives an overview of the Onsager and fundamental measure density functional theories, and presents the two-particle direct correlation function for isotropic states of circular platelets, self-consistency equations derived from the theory, and an isotropic stability analysis. Section V shows results from all approaches and we conclude in Sec. VI.

II. INTEGRAL EQUATION THEORY

A. Ornstein-Zernike equation and closure relations

The Ornstein-Zernike (OZ) equation for a homogeneous fluid of axially symmetric molecules is [1,2]

$$h(1,2) = c(1,2) + \frac{\rho}{4\pi}\int d3c(1,3)h(3,2), \tag{1}$$

where $h(1,2)=g(1,2)-1$ is the total correlation function, $g(1,2)$ is the pair distribution function, $c(1,2)$ is the direct correlation function (DCF), and ρ denotes the number density. We have abbreviated $(\boldsymbol{r}_i,\boldsymbol{u}_i)$ as i, where $\boldsymbol{r}_i$ denotes the center of mass position, and $\boldsymbol{u}_i$ is a unit vector along the symmetry axis of particle coordinates $i=1,2,3$.

In order to determine $h(1,2)$ and $c(1,2)$, Eq. (1) must be supplemented by an approximate closure relation. To formulate such relations note first that the *exact* closure relation can be written as [2]

$$y(1,2) \equiv g(1,2)\exp[V(1,2)/k_BT] = \exp[\gamma(1,2) + b(1,2)], \tag{2}$$

where $y(1,2)$ is the cavity (or background) correlation function, $V(1,2)$ is the intermolecular pair potential, T is the temperature, k_B is Boltzmann's constant, $\gamma(1,2)=h(1,2)-c(1,2)$, and $b(1,2)$ is the bridge function. Equation (2) may be regarded as defining $b(1,2)$; the (approximate) closure relations can then be formulated as approximations to $b(1,2)$. In particular, the most well-known closures [1,2] correspond to:

$$b(1,2) = 0 \quad \text{(HNC)}, \tag{3}$$

$$b(1,2) = -\gamma(1,2) + \ln[1+\gamma(1,2)] \quad \text{(PY)}. \tag{4}$$

A more sophisticated closure relation than Eqs. (3) and (4) is based on the form of the bridge function introduced by Verlet [48]:

$$b(1,2) = -\frac{(1/2)\gamma(1,2)^2}{1+\alpha\gamma(1,2)}, \quad \alpha = 0.8 \quad \text{(VB)}. \tag{5}$$

For hard sphere fluids α has been proposed to depend on packing fraction $\eta=\rho v_{\text{mol}}$ [13,17,49,50], where v_{mol} is the particle volume. However, as $v_{\text{mol}}=0$ for the infinitely thin platelets considered in this work, we will only use Eq. (5) in the following.

An alternative route to approximating the bridge function is based on its virial expansion

$$b(1,2) = \sum_{n\geq 2}\rho^n \mathfrak{B}_n(1,2), \tag{6}$$

where $\mathfrak{B}_n(1,2)$ is the sum of the nth order bridge diagrams [2]. As in previous work [23] we go beyond the HNC Eq. (3) by truncating Eq. (6) after the lowest or next-to-lowest order term, in order to find a closed approximation for $b(1,2)$ via

$$b_2(1,2) = \rho^2\mathfrak{B}_2(1,2) \quad \text{(HNC+B2)}, \tag{7}$$

$$b_3(1,2) = \rho^2\mathfrak{B}_2(1,2) + \rho^3\mathfrak{B}_3(1,2) \quad \text{(HNC+B3)}. \tag{8}$$

B. Spherical harmonic expansions and coordinate frames

For numerical solution of the respective integral equation theories, but also for the analysis of simulation data, the two-particle functions are expanded in a basis set of rotational invariants [1,51]:

$$F(1,2) = \sum_{mn\ell} F^{mn\ell}(r)\Phi^{mn\ell}(\boldsymbol{u}_1,\boldsymbol{u}_2,\hat{\boldsymbol{r}}), \tag{9}$$

$$\Phi^{mn\ell}(\boldsymbol{u}_1,\boldsymbol{u}_2,\hat{\boldsymbol{r}}) = 4\pi\sum_{\mu\nu\lambda}\begin{pmatrix} m & n & \ell \\ \mu & \nu & \lambda \end{pmatrix} Y_{m\mu}(\boldsymbol{u}_1)Y_{n\nu}(\boldsymbol{u}_2) \times\sqrt{\frac{4\pi}{2\ell+1}}Y_{\ell\lambda}(\hat{\boldsymbol{r}}), \tag{10}$$

where $F(1,2)$ denotes the two-particle function under consideration and all vectors are expressed in an arbitrary "labo-

ratory frame:" $\hat{\boldsymbol{r}}$ is a unit vector pointing along the line of particle centers, r is the intermolecular distance, $\boldsymbol{u}_1$ and $\boldsymbol{u}_2$ are the orientations of the two molecules, $Y_{m\chi}(\cdot)$ are the spherical harmonics, and $\begin{pmatrix} m & n & \ell \\ \mu & \nu & \lambda \end{pmatrix}$ is the standard $3j$ symbol [1].

Some of the analysis is most conveniently performed in the "molecular frame" [1], where the z axis lies along the intermolecular (direction) vector $\hat{\boldsymbol{r}}$. With molecular orientation vectors $\boldsymbol{u}_1^\circ$ and $\boldsymbol{u}_2^\circ$ referring to this frame, the expansion (10) becomes

$$F(1,2) = 4\pi \sum_{mn\chi} F_{mn\chi}(r) Y_{m\chi}(\boldsymbol{u}_1^\circ) Y_{n\bar{\chi}}(\boldsymbol{u}_2^\circ), \tag{11}$$

where $\bar{\chi} = -\chi$. The two sets of coefficients, $F^{mn\chi}(r)$ in the laboratory frame and $F_{mn\chi}(r)$ in the molecular frame, are related through the χ transform and its inverse, given, respectively, by

$$F_{mn\chi}(r) = \sum_{\ell} \begin{pmatrix} m & n & \ell \\ \chi & \bar{\chi} & 0 \end{pmatrix} F^{mn\ell}(r), \tag{12}$$

$$F^{mn\ell}(r) = (2\ell+1) \sum_{\chi} \begin{pmatrix} m & n & \ell \\ \chi & \bar{\chi} & 0 \end{pmatrix} F_{mn\chi}(r). \tag{13}$$

C. Numerical implementation of the integral equations

The integral equations are solved using standard decomposition of the correlation functions into rotational invariants [6,52] as outlined in previous work [23]. The solution is calculated using the Newton iterative solver presented in Ref. [53]. In the numerical calculations, the correlation function expansions are truncated at $m_{\max} = n_{\max} = 8$ and the r coordinate is discretized onto a grid in steps of $0.01D$. The bridge diagrams corresponding to the lowest nonvanishing orders in density, ρ^2 and ρ^3, see Eqs. (7) and (8), were calculated using Monte Carlo integration [54,55], again as outlined in Ref. [23].

III. SIMULATION METHODS

The techniques we use to calculate $h(1,2)$, $c(1,2)$, and $y(1,2)$ are the same as used and described in detail in previous work [23] and so will only be briefly sketched here. However, due to the extremely rapid variation of the interparticle hard core potential at contact for the models studied here, the technique used to calculate $b(1,2)$ differs from previous work.

Components of the pair correlation function $g(1,2)$ in the molecular frame (Sec. II B) are calculated from simulation in the usual manner [56]:

$$g_{mn\chi}(r) = 4\pi g_{000}(r) \langle Y^*_{m\chi}(\boldsymbol{u}_1^\circ) Y^*_{n\bar{\chi}}(\boldsymbol{u}_2^\circ) \rangle_r, \tag{14}$$

where the star indicates complex conjugation, $g_{000}(r)$ is the pair distribution function of the particle centers, and the angular brackets denote an average over all pairs of molecules with a distance r apart.

From Eq. (14) and the fact that $h(1,2) = g(1,2) - 1$, it follows directly that $h_{mn\chi}(r) = g_{mn\chi}(r) - \delta_{m0}\delta_{n0}\delta_{\chi 0}$.

The OZ equation (1) is most conveniently solved in reciprocal space,

$$\tilde{h}(1,2) = \tilde{c}(1,2) + \frac{\rho}{4\pi} \int d\boldsymbol{u}_3 \tilde{c}(1,3) \tilde{h}(3,2), \tag{15}$$

where the tilde indicates a (three-dimensional) Fourier transform with respect to position $\boldsymbol{r}_i$. Inserting the molecular frame expansion (in Fourier space with k as argument) into this gives

$$\tilde{h}_{mn\chi}(k) - \tilde{c}_{mn\chi}(k) = (-1)^\chi \rho \sum_p \tilde{c}_{mp\chi}(k) \tilde{h}_{pn\chi}(k). \tag{16}$$

Two methods are used for the calculation of the cavity function $y(1,2)$. In the first method we obtain $y(1,2)$ by directly simulating a system containing two mutually noninteracting (cavity) particles [57]. To within a multiplicative constant, $y(1,2)$ is equal to $P_{\text{cav}}(1,2)/r^2$, where $P_{\text{cav}}(1,2)$ is the probability distribution function for the two cavity particles and r is their center-center distance. In order to sample $P_{\text{cav}}(1,2)$ efficiently, the r coordinate is divided into overlapping windows and a bias function, generated using a Wang-Landau algorithm [58,59], is applied within each window. In the second method, the cavity function is calculated through test-particle insertion using Henderson's equation [60],

$$y(0,1) = \exp(\mu_{\text{ex}}/k_{\text{B}}T) \left\langle \exp\left(-\sum_{j \geqslant 2}^{N} \frac{V(0,j)}{k_{\text{B}}T} \right) \right\rangle_{N,V,T}, \tag{17}$$

where 0 labels position and orientation of the test particle and μ_{ex} is the excess chemical potential obtained from test particle insertion [61], and the particle number N, system volume V, and temperature T are kept constant.

Once g, h, c, and y are known, the bridge function can be found from the exact closure relation (2). In previous work [21,23] differentiation of Eq. (2) was used to give a set of linear equations for the spherical harmonics coefficients of $\partial b(1,2)/\partial r$. Due to the rapid variation of the correlation functions as $r \to 0$ this method has proved to be unreliable for the present model. Instead the spherical harmonics coefficients $\psi_{mn\chi}(r)$ of $\ln y(1,2)$ are found directly from

$$\ln y(1,2) = 4\pi \sum_{m,n,\chi} \psi_{mn\chi}(r) Y_{m\chi}(\boldsymbol{u}_1^\circ) Y_{n\bar{\chi}}(\boldsymbol{u}_2^\circ). \tag{18}$$

The expansion coefficients of $y(1,2)$ may then be written as [20]

$$y_{mn\chi}(r) = \frac{1}{4\pi} \int d\boldsymbol{u}_1^\circ d\boldsymbol{u}_2^\circ \exp\Bigg(4\pi \sum_{m',n',\chi'} \psi_{m'n'\chi'}(r) \times Y_{m'\chi'}(\boldsymbol{u}_1^\circ) Y_{n'\bar{\chi}'}(\boldsymbol{u}_2^\circ) \Bigg) Y^*_{m\chi}(\boldsymbol{u}_1^\circ) Y_{n\bar{\chi}}(\boldsymbol{u}_2^\circ), \tag{19}$$

which may be taken to be the implicit definition of $\psi_{mn\chi}(r)$. The $\psi_{mn\chi}(r)$ are then fitted to the simulation results for $y_{mn\chi}(r)$ using a modified Newton scheme [62]. Components of the bridge function are found subsequently by subtraction,

$$b_{mn\chi}(r) = \psi_{mn\chi}(r) - h_{mn\chi}(r) + c_{mn\chi}(r). \tag{20}$$

The particles considered in the present work are hard, infinitely thin platelets of diameter D (which we use as the unit of length, $D=1$, in the following) as well as hard oblate spheroids with elongations $e=A/D=0.1$, 0.05, and 0.01. For obtaining results for $h(1,2)$, systems consisting of 2000–3500 molecules were simulated. Statistics for $h(1,2)$ were gathered over 4×10^6 MC sweeps (where one MC sweep consists of one attempted translation and one attempted rotation per molecule), divided into four subruns. The bin width was set to $\delta r=0.01D$ and the spherical harmonics expansions were truncated at $m_{\max}=8$. $y(1,2)$ was calculated using systems containing 500 molecules. For the direct calculation of $y(1,2)$, the r separation between the cavity molecules was divided up into intervals $r/D=[0.03,0.20]$, $[0.10,0.50]$, $[0.40,0.80]$, and $[0.70,1.10]$. Within each window a weight function was generated over typically 20–25 refinement cycles and then data for the cavity function was gathered over 20×10^6 MC sweeps divided into four subruns.

IV. DENSITY FUNCTIONAL THEORY

A. Minimization principle and free energy functional

Density functional theory (DFT) is a powerful tool used to describe the equilibrium structure and thermodynamics of molecular liquids, in particular in inhomogeneous situations [42]. The theory operates on the one-body level and hence is formulated using the density distribution $\rho(\mathbf{r}_1,\boldsymbol{u}_1)\equiv\rho(1)$ and a variational principle that states that the equilibrium density profile is that which minimizes the grand potential functional [42] and hence obeys

$$\frac{\delta\Omega([\rho(1)],\mu,V,T)}{\delta\rho(1)}=0, \tag{21}$$

with the grand potential expressed as a functional of the one-body density distribution,

$$\Omega([\rho(1)],\mu,V,T)=F_{\mathrm{id}}([\rho(1)],V,T)+F_{\mathrm{exc}}([\rho(1)],V,T)+\int d1\rho(1)[V_{\mathrm{ext}}(1)-\mu], \tag{22}$$

where $\int d1=\int_V d\mathbf{r}\int d\boldsymbol{u}$; the spatial integral is over the system volume V and the angular integral is over the unit sphere; $V_{\mathrm{ext}}(1)$ is an external potential (describing, e.g., walls or the influence of gravity on the system); in the following we consider only bulk properties and hence set $V_{\mathrm{ext}}(1)=0$; μ is the chemical potential; $F_{\mathrm{exc}}[\rho(1)]$ is the excess (over ideal gas) contribution to the free energy. The exact ideal gas free energy functional is given by

$$\beta F_{\mathrm{id}}[\rho(1)]=\int d1\rho(1)[\ln(\rho(1)\Lambda^3)-1], \tag{23}$$

where $\beta=1/(k_BT)$ and Λ is the (irrelevant) thermal wavelength, we set $\Lambda=D$ in the following; this is equivalent to fixing an arbitrary additive constant to the chemical potential, which does not affect any observable properties of the system. The excess free energy functional can be expanded in a virial series,

$$\beta F_{\mathrm{exc}}[\rho(1)]=-\frac{1}{2}\,\bullet\!\!-\!\!\bullet-\frac{1}{6}\,\bullet\!\!\triangle\!\!\bullet+O(\rho^4), \tag{24}$$

where each line represents a Mayer bond $f(1,2)$ and the filled circles are *field points* that indicate multiplication by the one-body density $\rho(i)$ and integration over the coordinates $\boldsymbol{r}_i$ and $\boldsymbol{u}_i$ $(i=1,2)$ [2]. For the case of hard core pair interactions $f(1,2)=-1$ if the particle pair overlaps, and zero otherwise. More explicitly, the second-order diagram in Eq. (24) is

$$\bullet\!\!-\!\!\bullet=\int d1\rho(1)\int d2\rho(2)f(1,2), \tag{25}$$

which is in Onsager theory [43] the only contribution to the excess free energy functional; third and higher order terms in density in Eq. (24) are neglected in this approach.

Rosenfeld's fundamental measure theory (FMT) is a nonperturbative approach that was developed originally for additive hard sphere mixtures (see Refs. [63,64]); generalizations to general convex shapes have been proposed [65,66]. This led to subsequent work [67,68]. In particular an FMT was constructed specifically for hard platelets with vanishing thickness [45]; this features the correct second virial term in the excess free energy functional, Eq. (25), as well as an approximate term of third order in density:

$$\beta F_{\mathrm{exc}}[\rho]=-\frac{1}{2}\,\bullet\!\!-\!\!\bullet+\frac{1}{3\pi^2}\int d\mathbf{x}\int d\boldsymbol{u}_1\int d\boldsymbol{u}_2\int d\boldsymbol{u}_3\times n_2^{\mathrm{D}}(\mathbf{x},\boldsymbol{u}_1)n_2^{\mathrm{D}}(\mathbf{x},\boldsymbol{u}_2)n_2^{\mathrm{D}}(\mathbf{x},\boldsymbol{u}_3)|(\boldsymbol{u}_1\times\boldsymbol{u}_2)\cdot\boldsymbol{u}_3|, \tag{26}$$

where $\times$ denotes the vector product, such that $(\boldsymbol{u}_1\times\boldsymbol{u}_2)\cdot\boldsymbol{u}_3$ is the scalar triple product; note that the modulus in Eq. (26) renders the integration kernel non-negative. The weighted density $n_2^{\mathrm{D}}(\boldsymbol{r},\boldsymbol{u})$ is related to the bare one-body density via spatial convolution,

$$n_2^{\mathrm{D}}(\mathbf{x},\boldsymbol{u})=\int d\boldsymbol{r}w_2^{\mathrm{D}}(\mathbf{x}-\mathbf{r},\boldsymbol{u})\rho(\mathbf{r},\boldsymbol{u}), \tag{27}$$

where $w_2^{\mathrm{D}}(\mathbf{r},\boldsymbol{u})$ is a weight function that describes the platelet surface, given by

$$w_2^{\mathrm{D}}(\mathbf{r},\boldsymbol{u})=2\Theta(R-|\mathbf{r}|)\delta(\mathbf{r}\cdot\boldsymbol{u}), \tag{28}$$

where $\Theta(\cdot)$ is the Heaviside step function and $\delta(\cdot)$ is the (one-dimensional) Dirac delta distribution. We have kept the notation of [45] where the superscript D refers to the species (*disk*), but have simplified the expression by including the scalar triple product of orientations directly in Eq. (26) rather than to use it to define a further weighted density n_2^{DDD} [45]. Note that $w_2^D(1)$ is a quantity of dimension (length)$^{-1}$ and that its spatial integral, $\xi_2=\int d\boldsymbol{r}w_2(\boldsymbol{r},\boldsymbol{u})=\pi D^2/2$, equals the total platelet surface area (i.e., the sum of that of the "front" and of the "back" side), independent of orientation $\boldsymbol{u}$.

B. Bulk two-body direct correlation function for hard platelets

In the following we calculate the two-particle direct correlation function, $c(1,2)$, for bulk isotropic states, starting

from the excess free energy functional defined above. Note that the DCF, as obtained from a second functional derivative of the excess free energy functional (24), is given by

$$c(1,2) = -\beta \frac{\delta^2 F_{\text{exc}}[\rho]}{\delta\rho(1)\delta\rho(2)}\bigg|_{\rho=\text{const}}. \tag{29}$$

Inserting Eq. (24) into Eq. (29) yields the virial expansion of the DCF,

$$c(1,2) = f(1,2) + \rho \int d3 f(1,2) f(1,3) f(2,3) + O(\rho^2) \tag{30}$$

$$= \quad + \quad + O(\rho^2), \tag{31}$$

where the open circles represent root points not to be integrated over.

We next use the FMT and calculate the second functional derivative of Eq. (26) giving here only a sketch of the derivation. For an extensive set of similar calculations including detailed steps the reader is referred to Ref. [45]. Using the definition of the weighted density (27) it is straightforward to obtain

$$c(1,2) = \quad - \frac{2\rho}{\pi^2} \int \frac{d\boldsymbol{u}_3}{4\pi} \int d\boldsymbol{r}_3 \int d\boldsymbol{x} w_2^{\text{D}}(\boldsymbol{r}_1 - \boldsymbol{x}, \boldsymbol{u}_1) \times w_2^{\text{D}}(\boldsymbol{r}_2 - \boldsymbol{x}, \boldsymbol{u}_2) w_2^{\text{D}}(\boldsymbol{r}_3 - \boldsymbol{x}, \boldsymbol{u}_3) |(\boldsymbol{u}_1 \times \boldsymbol{u}_2) \cdot \boldsymbol{u}_3|. \tag{32}$$

The integrand in Eq. (32) vanishes for configurations where the three particles possess a common geometric intersection, which will in general (when $\boldsymbol{u}_1$, $\boldsymbol{u}_2$, and $\boldsymbol{u}_3$ are pairwise nonparallel) be a single point that is the intersection of the three planes each of which is due to the delta function in the weight function (28). For such cases carrying out the spatial integral over $\boldsymbol{x}$ yields $1/|(\boldsymbol{u}_1 \times \boldsymbol{u}_2) \cdot \boldsymbol{u}_3|$, which precisely cancels the scalar triple vector product in Eq. (32); the cancellation of undesirable divergences is the *raison d'être* of the scalar triple product in Eq. (26); see Ref. [45] for a discussion.

The shapes of particles 1 and 2 possess an intersection line with orientation $\boldsymbol{u}_1 \times \boldsymbol{u}_2$ and length $l(1,2)$. The integration over $\boldsymbol{r}_3$ in Eq. (32) yields the overlap (excluded) volume of this line and the disk with orientation $\boldsymbol{u}_3$; this results in a skewed cylinder with volume $l(1,2)\cos(\theta_3)\pi D^2/4$, where θ_3 is the (polar) angle between $\boldsymbol{u}_1 \times \boldsymbol{u}_2$ and $\boldsymbol{u}_3$. The $\boldsymbol{u}_3$ integration can be performed as $\int d\boldsymbol{u}_3 = \int d\theta_3 \sin\theta_3 \int d\phi_3 = 2\pi \int_{-1}^{1} d\cos\theta_3$. Hence the $\boldsymbol{u}_3$-averaged volume of the skewed cylinder is $l(1,2)\pi D^2/8 = l(1,2)\mathcal{A}/2$ where the factor $1/(4\pi)$ in Eq. (32) was taken into account and $\mathcal{A} = \xi_2/2 = \pi D^2/4$ is the platelet facial area. Agglomerating three factors of 2 from Eq. (28) yields

$$c(1,2) = f(1,2) - \frac{2D^2\rho}{\pi} l(1,2), \tag{33}$$

where $l(1,2)$ is the length of the intersection line of platelets 1 and 2. The constant $2D^2/\pi$ may be written as $8\mathcal{A}/\pi^2 = 0.810\,569\mathcal{A}$.

C. Self-consistency equation for the orientation distribution function

The minimization principle Eq. (21) for the grand potential functional leads to an Euler-Lagrange equation for the orientation distribution function (ODF). In order to consider the limit of stability of the isotropic phase with respect to nematic ordering, we next give the explicit self-consistency equation for the ODF in the nematic phase. For spatially homogeneous states, the one-body density $\rho(1)$ does not depend on position $\mathbf{r}$ and for the case of uniaxial nematics considered here depends only on the polar angle θ with respect to the nematic director but not on the azimuthal angle. Hence such states are characterized by $\rho(1) = \rho\Psi(\theta)$, where ρ (without argument) denotes the bulk number density and $\Psi(\theta)$ is the ODF. There is inversion symmetry under $\boldsymbol{u} \to -\boldsymbol{u}$ (unlike in a ferromagnetic phase for example, where this symmetry is broken) implying that $\Psi(\theta) = \Psi(\theta - \pi)$. We use a dimensionless density $c = \rho D^3$.

The method is based on Ref. [69] and we follow closely the very useful "recipe" of [70]. Note that $\int d\boldsymbol{u} = \int_0^{2\pi} d\phi \int_0^{\pi} d\theta \sin\theta$. For spatially homogeneous states, the second order contribution to the free energy may be written as

$$\frac{\beta F_{\text{exc}}^{(2)}[\rho(1)]}{V} = -\frac{1}{2} \int d\boldsymbol{u}_1 \int d\boldsymbol{u}_2 \rho(\boldsymbol{u}_1)\rho(\boldsymbol{u}_2) A'(\boldsymbol{u}_1, \boldsymbol{u}_2), \tag{34}$$

where $V = \int d\mathbf{r}$ is the system volume and the kernel is $A'(\boldsymbol{u}_1, \boldsymbol{u}_2) = \int d\mathbf{r} f(\mathbf{r}, \boldsymbol{u}_1, \boldsymbol{u}_2)$, and the superscript i of $F_{\text{exc}}^{(i)}$ represents the order in density. Carrying out this spatial integral one arrives at

$$\frac{\beta F_{\text{exc}}^{(2)}[\rho(1)]D^3}{V} = 2\pi^2 c^2 \int_0^{\pi/2} d\theta_1 \sin\theta_1 \int_0^{\pi/2} d\theta_2 \sin\theta_2 \times K(\theta_1, \theta_2)\Psi(\theta_1)\Psi(\theta_2), \tag{35}$$

where θ_1 and θ_2 are the polar angles of two platelets. Those are coupled by the kernel

$$K(\theta_1, \theta_2) = \int_0^{2\pi} d\phi \sqrt{1 - (\cos\theta_1 \cos\theta_2 + \sin\theta_1 \sin\theta_2 \cos\phi)^2}, \tag{36}$$

with the integrand being $|\sin\gamma|$ where γ is the angle between the normals of the two platelets with relative azimuthal angle ϕ.

To the exact third virial level

$$\frac{\beta F_{\text{exc}}^{(3)}[\rho(1)]}{V} = \int d\boldsymbol{u}_1 \int d\boldsymbol{u}_2 \int d\boldsymbol{u}_3 B(\boldsymbol{u}_1, \boldsymbol{u}_2, \boldsymbol{u}_3) \times \rho(\boldsymbol{u}_1)\rho(\boldsymbol{u}_2)\rho(\boldsymbol{u}_3), \tag{37}$$

where

$$B(\boldsymbol{u}_1,\boldsymbol{u}_2,\boldsymbol{u}_3) = -\frac{1}{6V}\int d\boldsymbol{r}_1 \int d\boldsymbol{r}_2 \int d\boldsymbol{r}_3 f(\boldsymbol{r}_1-\boldsymbol{r}_2,\boldsymbol{u}_1,\boldsymbol{u}_2) \times f(\boldsymbol{r}_1-\boldsymbol{r}_3,\boldsymbol{u}_1,\boldsymbol{u}_3) f(\boldsymbol{r}_2-\boldsymbol{r}_3,\boldsymbol{u}_2,\boldsymbol{u}_3). \quad (38)$$

Instead of dealing with the exact expression, the FMT functional amounts to approximating $B(\boldsymbol{u}_1,\boldsymbol{u}_2,\boldsymbol{u}_3)$ by

$$B'(\boldsymbol{u}_1,\boldsymbol{u}_2,\boldsymbol{u}_3) = \frac{(\xi_2)^3}{3\pi^2}|(\boldsymbol{u}_1\times\boldsymbol{u}_2)\cdot\boldsymbol{u}_3|; \quad (39)$$

recall that $\xi_2^D = 2\pi R^2$ is the fundamental measure corresponding to the platelet surface. Choosing coordinates such that $\boldsymbol{u}_1=(\sin\theta_1,0,\cos\theta_1)$, $\boldsymbol{u}_2=(\cos\theta_2\sin\theta_2,\sin\phi_2\sin\theta_2,\cos\theta_2)$, and $\boldsymbol{u}_3=(\cos\theta_3\sin\theta_3,\sin\phi_3\sin\theta_3,\cos\theta_3)$ allows us to write more explicitly

$$\frac{\beta F_{\mathrm{exc}}^{(3)} D^3}{V} = \frac{2}{3}\pi^2 c^3 \int_0^{\pi/2} d\theta_1 \sin\theta_1 \int_0^{\pi/2} d\theta_2 \sin\theta_2 \int_0^{\pi/2} d\theta_3 \times \sin\theta_3 L(\theta_1,\theta_2,\theta_3)\Psi(\theta_1)\Psi(\theta_2)\Psi(\theta_3), \quad (40)$$

where the kernel that couples the three polar angles θ_1, θ_2, and θ_3 is given by

$$L(\theta_1,\theta_2,\theta_3) = \int_0^{2\pi} d\phi_2 \int_0^{2\pi} d\phi_3 |\sin\theta_1(\sin\phi_2\sin\theta_2\cos\theta_3 - \cos\theta_2\sin\phi_3\sin\theta_3) + \cos\theta_1(\cos\phi_2\sin\theta_2\sin\phi_3\sin\theta_3 - \sin\phi_2\sin\theta_2\cos\phi_3\sin\theta_3)|. \quad (41)$$

The minimization principle (21) yields an Euler-Lagrange equation in the form of an implicit self-consistency equation. In order to determine the ODF for nematic states numerical work is required. Some analytic progress can be made with a stability analysis of the isotropic state (presented below). For Onsager theory the resulting self-consistency equation is given by

$$\Psi(\theta_1) = \frac{1}{Z}\exp\left(-\pi c\int_0^{\pi/2} d\theta_2 \sin\theta_2 K(\theta_1,\theta_2)\Psi(\theta_2)\right), \quad (42)$$

where Z is a normalization constant that ensures that $4\pi\int_0^{\pi/2}\sin\theta\Psi(\theta)d\theta=1$. For FMT,

$$\Psi(\theta_1) = \frac{1}{Z}\exp\left(-\pi c\int_0^{\pi/2} d\theta_2 \sin\theta_2 K(\theta_1,\theta_2)\Psi(\theta_2) - \frac{\pi c^2}{2}\int_0^{\pi/2} d\theta_2 \sin\theta_2 \int_0^{\pi/2} d\theta_3 \sin\theta_3 \times L(\theta_1,\theta_2,\theta_3)\Psi(\theta_2)\Psi(\theta_3)\right). \quad (43)$$

We will use Eqs. (42) and (43) in the following to investigate the limit of stability of the isotropic phase.

D. Bifurcation from the isotropic solution

It is well established that Onsager's theory for rods predicts an isotropic-symmetry-breaking bifurcation [71]. The nematic solution branches off from the isotropic state at the bifurcation point. This branch is metastable and eventually connects to the stable branch of the nematic solution in a smooth fashion. For example, the metastable branch was calculated for rods in [71] and extended to a class of liquid crystal models in [72]. Here we perform a similar bifurcation analysis for platelets, first using Onsager theory and then FMT. We do not proceed to find the entire metastable branch here but focus on finding the bifurcation density c^*. The isotropic phase is unstable with respect to an infinitesimally anisotropic perturbation for $c>c^*$; hence c^* represents the upper limit of stability of the isotropic phase. This is larger than the isotropic coexistence density. Substituting $\Psi(\theta)=[1+\epsilon P_2(\cos\theta)]/4\pi$ into the free energy functional, where ϵ is a small parameter that measures the strength of the pertubation, yields $F_{\mathrm{iso}}(c)+a(c)\epsilon^2$, where $F_{\mathrm{iso}}(c)$ is the free energy of the isotropic state, and $P_2(\cos\theta)=\frac{1}{2}(3\cos^2\theta-1)$ is the second Legendre polynomial in $\cos\theta$. The requirement that $a(c^*)=0$ yields the bifurcation density c^* with $a(c<c^*)>0$ and $a(c>c^*)<0$. The choice of the angular dependence of the perturbation, $P_2(\cos\theta)/4\pi$, is made because this function is orthogonal to the isotropic ODF and represents the simplest type of nematic orientational ordering. Table I lists the bifurcation densities c^* for Onsager theory and FMT. For both theories, c^* lies between the isotropic and nematic phase coexistence densities, c_I and c_N, respectively. Note that the coexistence range of densities between the isotropic and nematic phases is smaller in FMT such that $c_I<c^*<c_N$, and that the bifurcation density is much lower than in Onsager theory. The same value for c^* is found independently via consideration of the Kerr coefficient [see Eq. (44) below] using the FMT direct correlation function (33) as input, providing a valuable consistency check.

TABLE I. Isotropic and nematic coexistence densities c_I and c_N as well as bifurcation density c^* at which the isotropic phase becomes unstable, as obtained from Onsager theory and fundamental measure theory.

Theory	c_I	c^*	c_N
Onsager	5.328	6.485	6.792
FMT	3.344	3.472	3.680

V. RESULTS

A. Equation of state and isotropic stability

In Fig. 1(a) results are shown for the equation of state of hard, infinitely thin, circular platelets. In order to scrutinize the excess contribution to the total pressure P we plot the scaled form $[P/(\rho k_B T)-1]/\rho$ as a function of the density ρ (scaled with the volume D^3). In this representation truncating the equation of state at the second virial level (as in Onsager theory) yields a constant with respect to density, equal to the second virial coefficient, $\pi^2/16=0.616\,85$ for the present model. By definition, this is exact for $\rho\to 0$. Upon increasing density the simulation results indicate an (expected) increase due to additional, higher than second order in density, con-

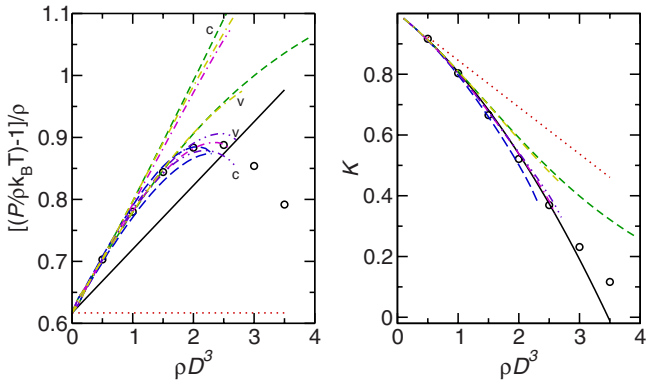

FIG. 1. (Color online) Left: equation of state $[(P/\rho k_B T)-1]/\rho$, for thin hard platelets. Right: Isotropic-nematic stability coefficient K. Fundamental measure theory (black, full line), Onsager (exact second virial) theory (red, dotted line), PY (green, dashed-line), HNC (blue, long-dashed line), HNC+B2 (magenta, dot-dashed line), HNC+B3 (violet, double-dot-dashed line), VB (gold, dot-double-dashed line), and MC (symbols). For the IET equations of state we show results of both the virial (v) and compressibility (c) routes to the equation of state.

tributions to the pressure. However, quite remarkably, a maximum of about 0.9 is reached at a density of 2.5 (significantly below the isotropic coexistence density $\rho D^3=3.68$), and a decrease occurs upon increasing the density further. All IETs are very good at capturing the initial increase at low densities, in near perfect agreement with simulation results up to $\rho D^3 \lesssim 1$. However, only the HNC based closures reproduce the nonmonotonic behavior observed in simulations. HNC+B3 theory [Eq. (8)] gives the best overall agreement between simulation and theory and also displays the smallest discrepancy between results from the virial and the compressibility routes. However, we can find only solutions for densities $\rho D^3 \lesssim 2.7$, which unfortunately prohibits the use of this approach to study states near isotropic-nematic coexistence. Pure HNC and HNC+B2 [Eq. (7)] (virial route only) also agree well with simulations, but fail to find a solution at high densities. Both PY and Verlet bridge (VB) approximations give increasingly poor performance upon increasing ρ and lead to significant overestimates for the excess pressure at high densities.

FMT predicts a linear dependence on density, as expected from the structure of the excess free energy including second and third order contributions in density. However, as it does not feature the exact third virial coefficient, the slope at small densities differs quite significantly from the simulation results. It is noticeable that the maximum in the equation of state (EOS) data seen in simulation is marginally predicted by HNC, HNC+B3 and HNC+B2 (virial only) EOS, however, the loss of solutions for IET in the vicinity of the maximum prevents a full exploration of this feature.

In Fig. 1(b) we display results for the Kerr coefficient [73,74], defined as

$$K = 1 - \frac{\rho}{\sqrt{5}} \tilde{c}^{220}(k=0), \tag{44}$$

where $\tilde{c}^{220}(k=0)=4\pi\int_0^\infty dr r^2 c^{220}(r)$ is the Fourier transform of the relevant DCF component $c^{220}(r)$. The Kerr coefficient plays an important role in assessing the stability of the isotropic phase, which is stable (unstable) with respect to an infinitesimal nematic perturbation if $K>0$ ($K<0$). Note that $K=0$ determines the limit of stability of the isotropic phase, not the thermodynamic coexistence density [6]. Onsager theory predicts K to decrease from its limiting value of unity at $\rho=0$ in a linear fashion as ρ increases. This is a direct consequence of Eq. (44) and the fact in Onsager theory $c(1,2)=f(1,2)$, independent of ρ. The simulation results reproduce the variation of K with ρ at low densities, but tend to deviate quickly and display a more pronounced decrease of K with increasing density. Initially the curvature is small and negative. At a density similar to that where the maximum in the scaled excess pressure occurs, a point of inflection can be gleaned from the data and the curvature becomes positive for larger values of ρ.

The performance of the various integral equation theories is similar to that observed for the case of the equation of state, with all closures reproducing the inital slope of Onsager theory and PY and VB performing worse than the various HNC versions in predicting a stronger than linear decay upon increasing density. While we have not attempted to extrapolate quantitatively the simulation results to the density at which $K=0$, it can be inferred from Fig. 1 that this would happen at around $\rho D^3=4$; as expected this value lies above that of the isotropic state at coexistence, $\rho D^3=3.68$ [24,25]. In Onsager theory the zero occurs at $\rho_{\mathrm{Kerr}}^{\mathrm{Ons}} D^3=6.49$, again higher than the corresponding value of the isotropic coexistence density, $\rho_{\mathrm{I}}^{\mathrm{Ons}} D^3=5.35$ [24], both significantly overestimating the simulation results. The result from FMT is comparable to those from integral equation theories at low densities, slightly overestimates K at intermediate densities, and agrees again reasonably well at high densities, although it fails to capture the change in curvature observed in the simulations and hence gives a slightly too low value for the instability density of $\rho_{\mathrm{Kerr}}^{\mathrm{FMT}} D^3=3.47$. This value is again higher than the corresponding value for the isotropic coexistence density $\rho_{\mathrm{I}}^{\mathrm{FMT}} D^3=3.34$ [45]. Hence the observation that the theory gives slightly too low values for the phase transition densities is reflected in the behavior of ρ_{Kerr}.

In conclusion the results for the equation of state and the variation of the Kerr coefficient with density indicate that all theories improve significantly over the simple Onsager approach. However, at high densities, close to the isotropic-nematic phase transition, subtle effects are observed in simulations, such as a change in curvature of K and a decrease in the scaled excess pressure. These effects are consistent with a physical interpretation of a "loss of interactions" in the system, such that the pressure in the isotropic state is lower and its region of stability is larger than what a simple extrapolation from the low-density behavior would suggest. Whether this is indicative of nematic preordering in the fluid remains speculation at this point. We will proceed next to investigate the structure on the pair level.

B. Direct correlation function

Results for the components of $c(1,2)$ in the expansion in spherical harmonics, $c_{mn\chi}(r)$ [see Eqs. (9) and (12) with

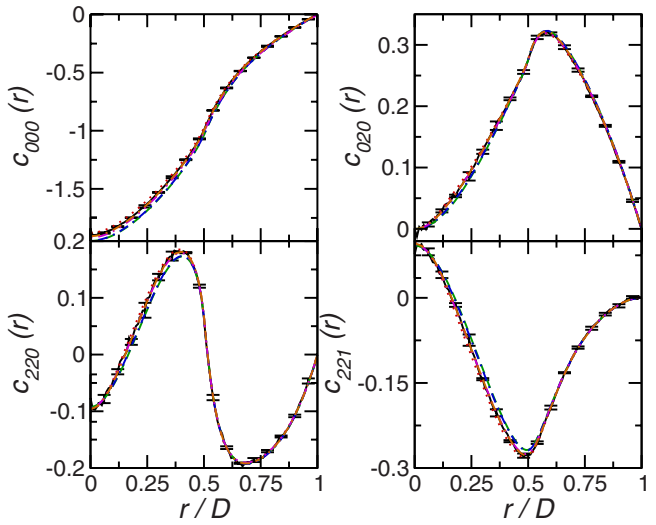

FIG. 2. (Color online) Direct correlation function components $c_{mn\chi}(r)$ for $mn\chi$=000, 020, 220, and 221, as a function of distance r/D for hard platelets at density ρD^3=1.0. Simulation results for hard platelets are the solid line (online: black), IET results using HNC closure are shown by the dotted line, PY by the dashed line, Verlet bridge by the dot-dashed line, HNC+B2 by the double-dot-dashed line, and HNC+B3 by the dot-double-dashed line (online: red, green, blue, magenta, and orange respectively).

$F(1,2)=c(1,2)$], obtained from integral equation theory with the different closures, are shown in Figs. 2–4. At low density, $\rho D^3=1$, all closures give excellent agreement with the simulation result, with the HNC closure with added virial bridge function (HNC+B2 and HNC+B3) yielding the best agreement. PY and the Verlet bridge function approximation perform marginally worse. Upon increasing the density, $\rho D^3=2$ (Fig. 3), both HNC closures remain more accurate than the other approximations. It is noticeable that no systematic improvement upon adding additional bridge function terms is observed; for some components [e.g., $c_{000}(r)$], the HNC closure yields better agreement with the simulation data than

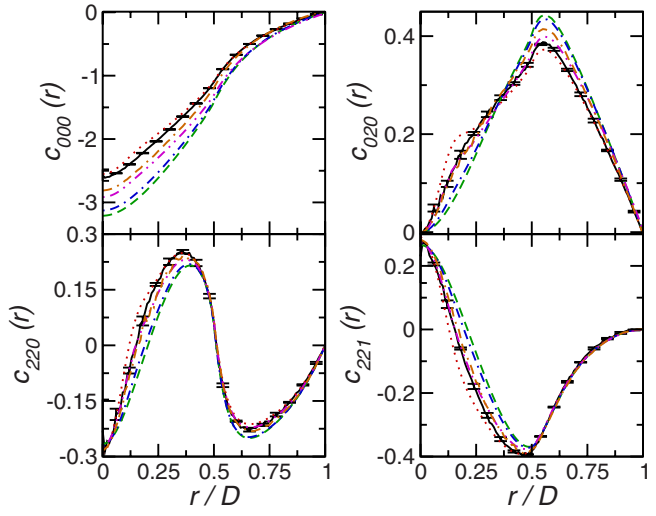

FIG. 3. (Color online) Direct correlation function components for hard platelets density ρD^3=2.0. Symbols are as in Fig. 2.

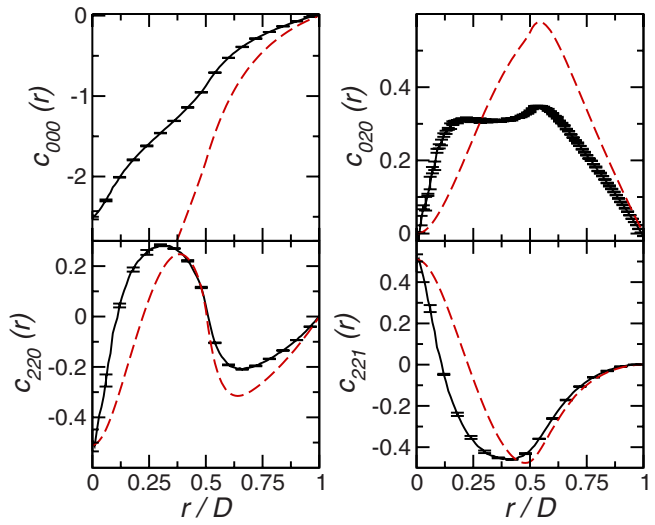

FIG. 4. (Color online) Direct correlation function components for hard platelets density ρD^3=3.0. Simulation results for hard platelets are shown by the solid line (online: black), IET results using PY closure are shown by dashed line (online: red).

either HNC+B2 or HNC+B3. In order to obtain a systematic improvement, extension to higher order in the bridge diagrams would possibly be required. The Verlet bridge approximation performs marginally better than the PY closure. The superior performance of the HNC closures over the Verlet bridge function method is in contrast to what was found in studies of moderately prolate and oblate spheroids and their mixtures [21,22]. Despite displaying the poorest quantitative agreement with the simulation data of all integral equations considered, the PY closure is the only approximation to give a solution for $\rho D^3 \gtrsim 2.7$); all other closures fail to converge.

Shown in Fig. 5 are selected components of the DCF for the hard platelet and oblate spheroid fluids at ρD^3=1.0. The DCF components for the oblate spheroids are qualitatively similar to those of the hard platelets, with the agreement improving as the elongation decreases. Also shown are DCF components calculated from FMT. For this density this largely shows good agreement with the simulation DCF, although it generally underestimates it. Earlier versions of FMT predict (incorrectly) that apart from the $c_{000}(r)$ component $c_{mn\chi}(r)\to 0$ as $r\to 0$ due to its relation to the Mayer function [18] [at $r=0$ all possible orientations of the molecules result in overlap, so the components $f_{mn\chi}(r=0)=\int d\boldsymbol{u}_1 d\boldsymbol{u}_2 f(1,2) Y^*_{m\chi}(\boldsymbol{u}_1) Y^*_{n\bar{\chi}}(\boldsymbol{u}_2) = -\int d\boldsymbol{u}_1 d\boldsymbol{u}_2 Y^*_{m\chi}(\boldsymbol{u}_1) Y^*_{n\bar{\chi}}(\boldsymbol{u}_2) = 0$ for $m,n\neq 0$]. The current FMT possesses the same defect, due to the fact that in Eq. (33) the intersection length of two disks $l(1,2)\to D$ for $r\to 0$, independent of the orientations of particles 1 and 2.

DCF components for higher densities are shown in Figs. 6–8. It is noticeable that the variation of the $c_{mn\chi}(r)$ with density is more complex than both for rod-shaped molecules and for less anisotropic discs [21]. The magnitude of $c_{000}(r)$ initially increases with density, but for $\rho D^3 \geqslant 2.5$ decreases. Similarly there are qualitative changes to the other components, most prominently the growth of second peak in $c_{020}(r)$

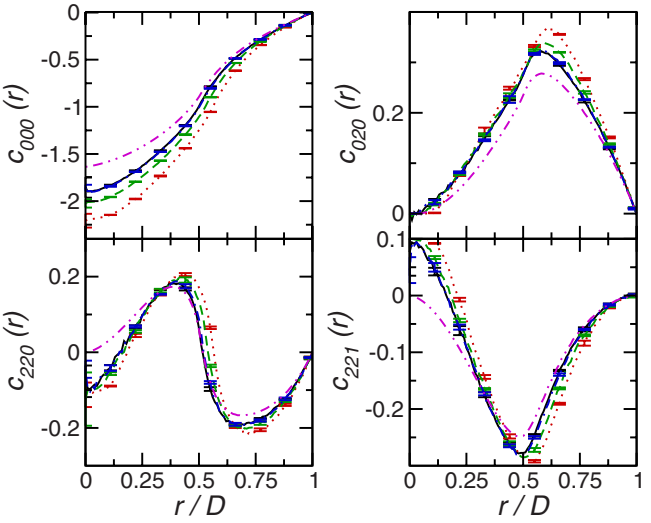

FIG. 5. (Color online) Direct correlation function components for hard platelets and oblate spheroids at density $\rho D^3=1.0$. Simulation results for hard platelets and hard spheroids with elongation $e=0.1$, $e=0.05$, and $e=0.01$ are shown by the solid, dotted, dashed, and dot-dashed lines (online: black, red, green, blue), respectively. DCF from FMT is denoted by the double-dot-dashed line (online: magenta).

at small separations $r\approx 0.15$. As for $\rho D^3=1.0$ the DCF components for the oblate spheroids show similar behavior to those of the hard platelets, with the similarity growing as e decreases. With increasing density the agreement between the simulation and the FMT results for the DCF components grows worse. In particular, as the DCF from FMT depends linearly on the density, it is unable to describe the nonmonotonic variation with density.

In order to further illustrate the structure on the pair level, we display results (from simulations only) for the second rank ($m=n=2$) components of the total correlation function, $h_{mn\chi}(r)$, in Fig. 9. Rich short-ranged oscillatory behavior is

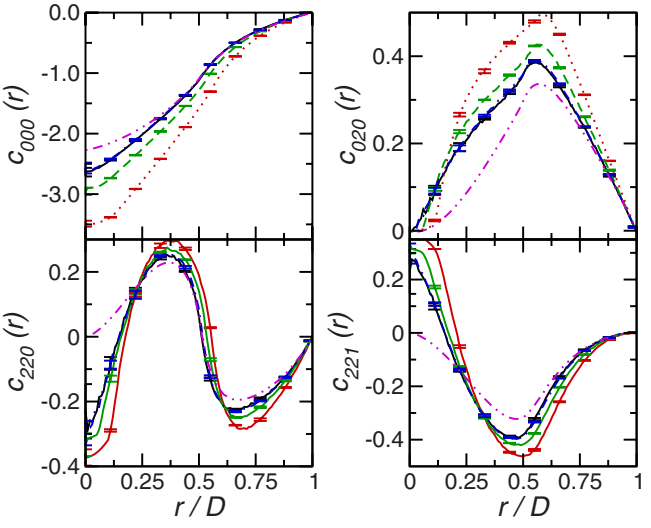

FIG. 6. (Color online) Direct correlation function components for hard platelets and oblate spheroids at $\rho D^3=2.00$. Symbols are as in Fig. 5.

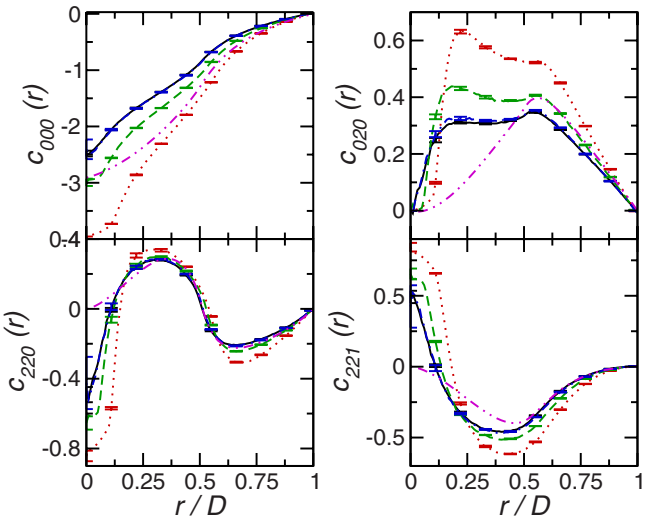

FIG. 7. (Color online) Direct correlation function components for hard platelets and oblate spheroids at $\rho D^3=3.00$. Symbols are as in Fig. 5.

apparent. Strikingly, the position of the first extremum moves towards smaller values upon increasing density. We attribute this to an increase in local parallel (nematiclike) ordering of the particles. On increasing density a pronounced tail develops in these components, indicating a growth in the orientational ordering as the isotropic-nematic transition is approached.

C. Bridge function

Shown in Figs. 10–12 are selected bridge function components for the hard platelet and oblate spheroid fluids. As for the DCF, the agreement between the hard platelet and spheroid bridge functions improves as the spheroid elongation decreases. The bridge function components also show nonmonotonic variation with density. Most noticeably the

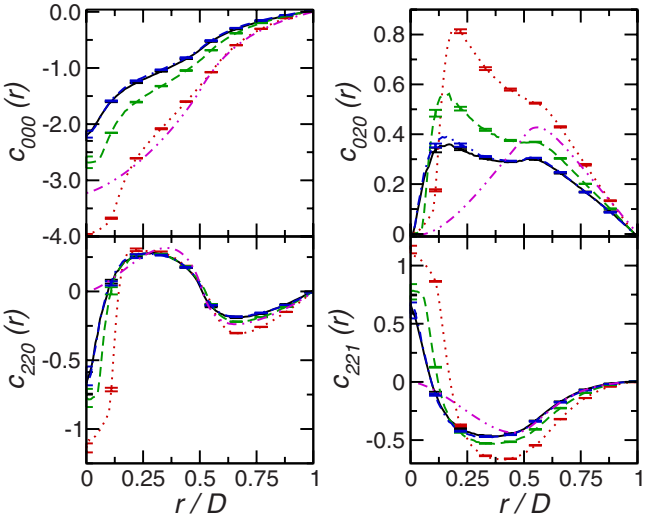

FIG. 8. (Color online) Direct correlation function components for hard platelets and oblate spheroids at $\rho D^3=3.50$. Symbols are as in Fig. 5.

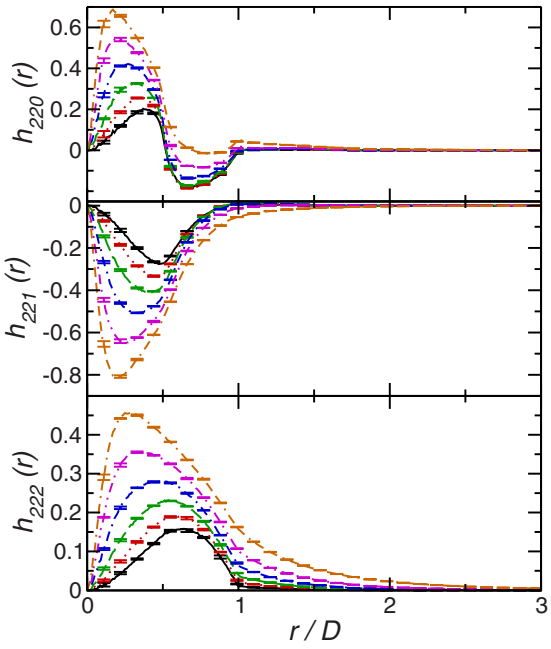

FIG. 9. (Color online) Second rank components of the total correlation function. Data for $\rho D^3=1.00$ denoted by the solid line, $\rho D^3=1.50$ by the dotted line, $\rho D^3=2.00$ by the dashed line, $\rho D^3=2.50$ by the dot-dashed line, $\rho D^3=3.00$ by the double-dot-dashed line, and $\rho D^3=3.5$ by the dot-double-dashed line (online black, red, green, blue, magenta, orange respectively).

$b_{000}(r)$ component changes sign with increasing density for the hard platelets and the $e=0.05$ and $e=0.01$ spheroids.

At low density (Fig. 10) the bridge function calculated from the virial expansion, for both first and second order in density, are in good agreement with the simulation bridge function components. On increasing density the agreement generally becomes worse. As for the DCF, increasing the order of expansion does not uniformly improve agreement with simulation, implying that higher order graphs in the expansion become increasingly important.

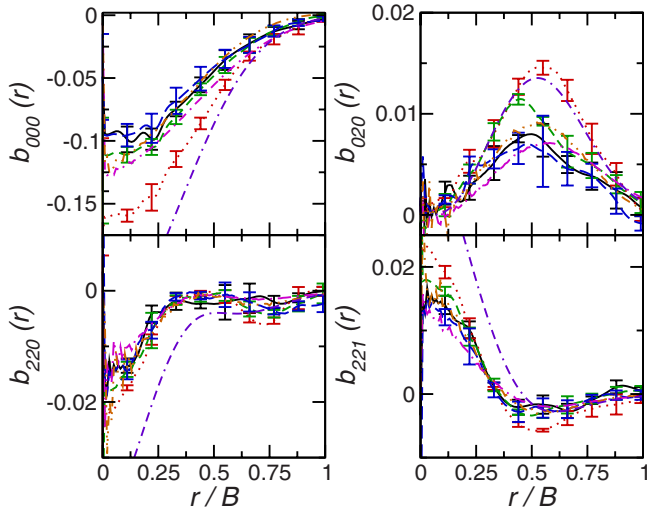

FIG. 10. (Color online) Bridge function components for hard platelets and oblate spheroids at $\rho D^3=1.00$. Simulation data for hard platelets and hard spheroids of elongation $e=0.10$, $e=0.05$, and $e=0.01$ are shown by solid, dotted, dashed, and long dashed lines (online: black, red, green, blue), respectively. Bridge function components found from second and third order virial expansion are shown by dot-dashed and double-dot-dashed lines (online: magenta, orange), respectively, and components of the Verlet bridge function are denoted by the double-dash-dot line (online: violet).

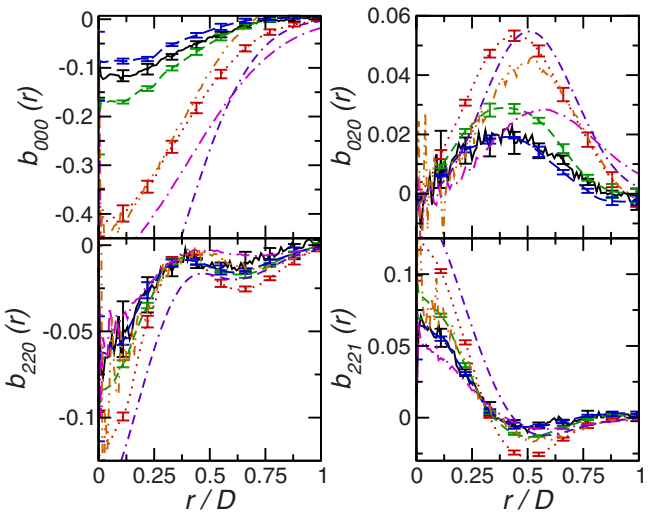

FIG. 11. (Color online) Bridge function components for hard platelets and oblate spheroids at $\rho D^3=2.00$. Symbols are as in Fig. 10.

D. Duh-Haymet plots

For convenience of presenting results below, we list in Table II eight relative arrangements of pairs of axially symmetric molecules, referred to by a single letter. The relative orientation angles are defined by $\cos\theta_1=\boldsymbol{u}_1\cdot\hat{\boldsymbol{r}}$, $\cos\theta_2=\boldsymbol{u}_2\cdot\hat{\boldsymbol{r}}$, and $\cos\phi=\hat{\boldsymbol{p}}_1\cdot\hat{\boldsymbol{p}}_2$ where $\hat{\boldsymbol{p}}_i$ is the unit vector in the direction $\boldsymbol{p}_i=\boldsymbol{u}_i\times\hat{\boldsymbol{r}}$. Orientation "*f*" corresponds to a face-to-face arrangement; "*s*" is side by side; "*t*" is a T shape; "*x*" is a

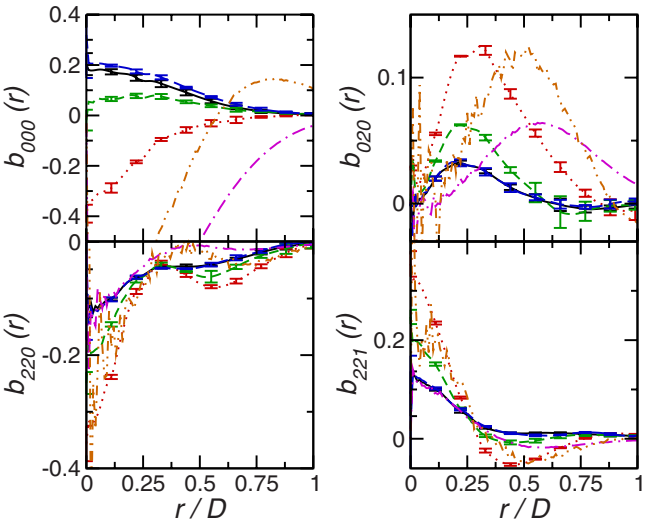

FIG. 12. (Color online) Bridge function components for hard platelets and oblate spheroids at $\rho D^3=3.00$. Symbols are as in Fig. 10.

TABLE II. Orientations of molecules relative to the center-center vector, used in the Duh-Haymet plots.

Orientation	*f*	*s*	*t*	*x*	*a*	*b*	*c*	*d*
ϕ (deg)	0	0	0	90	0	60	120	180
θ_1 (deg)	0	90	0	90	45	45	45	45
θ_2 (deg)	0	90	90	90	45	45	45	45

crossed arrangement where the molecular axes and the center-center vector are all mutually perpendicular. The remaining orientations "*a*"–"*d*" are less symmetrical: both molecular axes are tilted at 45° relative to the center-center vector, and four different twist angles ϕ are chosen in the sequence $\phi=0°$, 60°, 120°, 180°.

Most of the closure relations used in IET may be expressed as relations connecting $b(1,2)$ to $\gamma(1,2)=h(1,2)-c(1,2)$ [cf. Eq. (5)]. A convenient method for presenting this is through Duh-Haymet (DH) plots [75], where $b(1,2)$ is simply plotted as a function of $\gamma(1,2)$. DH plots for hard platelet and spheroid fluids at $\rho D^3=1.0$, $\rho D^3=2.0$, and $\rho D^3=3.0$ are shown in Figs. 13–15. At low density the curves for the hard platelets and oblate spheroids lie close to each other. As the density increases there is more scatter in the simulation results. In all cases it may be seen that curves for the different elongations lie very close to each other.

Also plotted in Figs. 13–15 are the PY and Verlet bridge functions [for $b^{\mathrm{HNC}}(1,2)=0$] for the hard platelet fluid. These both perform poorly, overestimating the magnitude of $b(1,2)$ at large $\gamma(1,2)$. The failure of the PY closure may be expected from previous results on molecular fluids [6,21]. The failure of the Verlet bridge may arise from the parameter $\alpha=0.8$ which was derived for the hard sphere fluid and is independent of density. Use of a density-dependent α has been shown to improve agreement between simulation and IET [21,22].

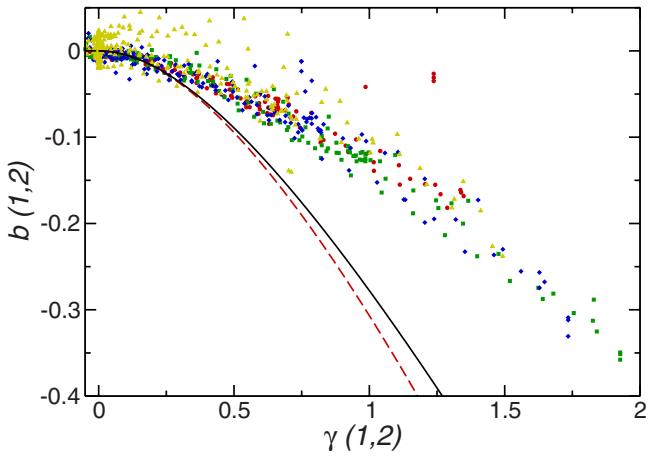

FIG. 13. (Color online) Duh-Haymet plot for hard platelets (circles, online red), and hard spheroids with elongations $e=0.1$ (squares, online green), $e=0.05$ (diamonds, online blue), and $e=0.01$ (triangles, online gold) at $\rho D^3=1.0$. The solid line shows MV bridge function and the dashed line shows the PY bridge function.

VI. CONCLUSIONS

In this paper the structure and thermodynamics of the hard platelet and highly oblate spheroid fluids in the isotropic phase have been studied. The equation of state data for hard platelets found from MC simulations shows anomalous behavior with increasing density. This anomalous behavior is not reproduced by IET with the PY or Verlet Bridge closures or by DFT. IET with the HNC and HNC+B3 closures, as well HNC+B2 (using the virial route), do capture this behavior, although they all fail to find a solution at densities just above this maximum. Likewise both the DCF and bridge function components show nonmonotonic variation with density. On decreasing spheroid elongation, the thermodynamic and correlation functions tend towards those of the infinitely thin platelets.

Comparison of the DCF and bridge function components found from simulation and theoretical approximations show that, in general, HNC-based closures [with either $b(1,2)=0$ or found from the low-density expansion] give the best agreement with simulation. By contrast, IET's using PY and Verlet closures perform poorly. Consideration of DH plots shows large discrepancies between the simulation and IET (PY and Verlet) bridge functions. Modification of the Verlet bridge function [Eq. (5)] to include a density dependent α may be expected to improve its performance, as is the case of hard spheroids of moderate elongations [21]. Also studied was a recently developed FMT-based density functional, from which the DCF was obtained via a second functional derivative, yielding a geometric interpretation of the term linear in density, as the length of the intersection line be-

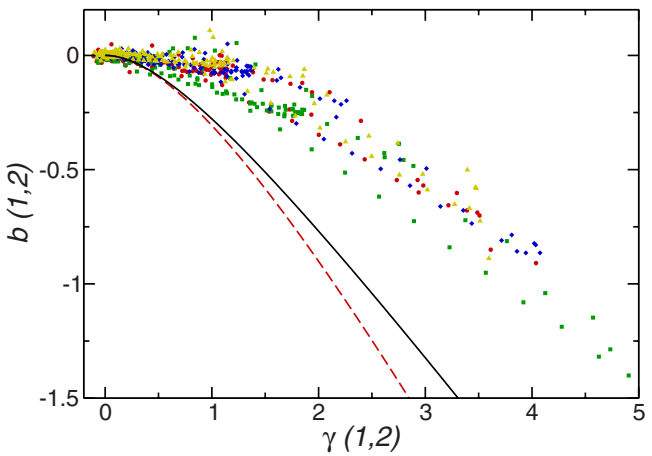

FIG. 14. (Color online) Duh-Haymet plot for hard platelets and hard spheroids at $\rho D^3=2.0$. Symbols are as in Fig. 13.

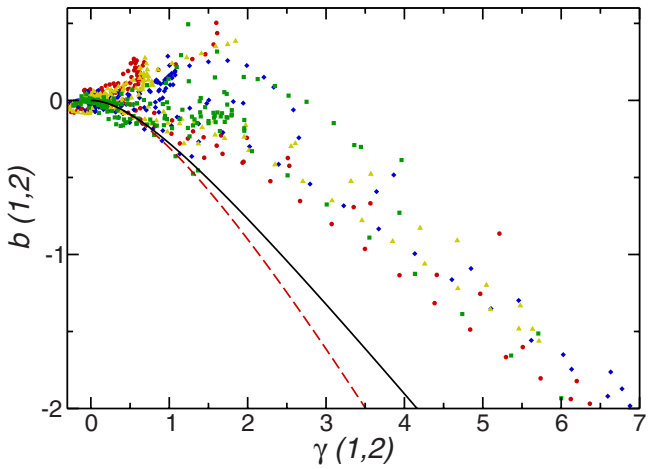

FIG. 15. (Color online) Duh-Haymet plot for hard platelets and spheroids at $\rho D^3=3.0$. Symbols are as in Fig. 13.

tween two platelets. This approximate DFT was shown to fail to reproduce all structural details, but to capture the main trends found in simulations.

As an outlook, it would be interesting to carry out a detailed study of the asymptotic decay of the pair correlations at large separation distances [76–78]. This would shed further light onto possible structural crossover from damped oscillatory to monotonic decay of density profiles at walls [46].

ACKNOWLEDGMENTS

M.S. and J.P. thank Chris Newton and Susanne Klein for useful discussions. Financial support from the EPSRC and HP Labs, Bristol is gratefully acknowledged. This work was supported by EPSRC Grant Nos. GR/S77240 and GR/S77103. Computational resources were provided by the Centre for Scientific Computing, University of Warwick and Manchester Computing, University of Manchester.

[1] C. G. Gray and K. E. Gubbins, *Theory of Molecular Fluids. 1. Fundamentals* (Clarendon Press, Oxford, 1984).
[2] J. P. Hansen and I. R. McDonald, *Theory of Simple Liquids*, 3rd ed. (Academic Press, London, 2006).
[3] F. J. Rogers and D. A. Young, Phys. Rev. A **30**, 999 (1984).
[4] S. Rast, P. H. Fries, and H. Krienke, Mol. Phys. **96**, 1543 (1999).
[5] J. M. Brader, J. Chem. Phys. **128**, 104503 (2008).
[6] A. Perera, P. G. Kusalik, and G. N. Patey, J. Chem. Phys. **87**, 1295 (1987).
[7] A. Perera and G. N. Patey, J. Chem. Phys. **89**, 5861 (1988).
[8] A. Chamoux and A. Perera, J. Chem. Phys. **108**, 8172 (1998).
[9] P. H. Fries and G. N. Patey, J. Chem. Phys. **82**, 429 (1985).
[10] A. Perera, P. G. Kusalik, and G. N. Patey, J. Chem. Phys. **89**, 5969 (1988).
[11] M. Letz and A. Latz, Phys. Rev. E **60**, 5865 (1999).
[12] R. C. Singh, J. Ram, and Y. Singh, Phys. Rev. E **54**, 977 (1996).
[13] S. Labík, A. Malijevský, and W. R. Smith, Mol. Phys. **73**, 87 (1991).
[14] S. Labík, A. Malijevský, and W. R. Smith, Mol. Phys. **73**, 495 (1991).
[15] R. Pospíšil, A. Malijevský, S. Labík, and W. R. Smith, Mol. Phys. **74**, 253 (1991).
[16] S. Labík, A. Malijevský, R. Pospíšil, and W. R. Smith, Mol. Phys. **74**, 261 (1991).
[17] R. Pospíšil, A. Malijevský, and W. R. Smith, Mol. Phys. **79**, 1011 (1993).
[18] M. P. Allen, C. P. Mason, E. de Miguel, and J. Stelzer, Phys. Rev. E **52**, R25 (1995).
[19] N. H. Phuong, G. Germano, and F. Schmid, J. Chem. Phys. **115**, 7227 (2001).
[20] E. Lomba, M. Lombardero, and J. L. F. Abascal, J. Chem. Phys. **90**, 7330 (1989).
[21] D. L. Cheung, L. Anton, M. P. Allen, and A. J. Masters, Phys. Rev. E **76**, 041201 (2007).
[22] D. L. Cheung, L. Anton, M. P. Allen, and A. J. Masters, Phys. Rev. E **77**, 011202 (2008).
[23] D. L. Cheung, L. Anton, M. P. Allen, and A. J. Masters, Phys. Rev. E **73**, 061204 (2006).
[24] D. Frenkel and R. Eppenga, Phys. Rev. Lett. **49**, 1089 (1982).
[25] R. Eppenga and D. Frenkel, Mol. Phys. **52**, 1303 (1984).
[26] M. A. Bates, J. Chem. Phys. **111**, 1732 (1999).
[27] S. Chandrasekhar and G. S. Ranganath, Rep. Prog. Phys. **53**, 57 (1990).
[28] S. Kumar, Liq. Cryst. **31**, 1037 (2004).
[29] R. J. Bushby and O. R. Lozman, Curr. Opin. Colloid Interface Sci. **7**, 343 (2002).
[30] F. M. van der Kooij, K. Kassapidou, and H. N. W. Lekkerkerker, Nature (London) **406**, 868 (2000).
[31] F. M. van der Kooij, D. van der Beek, and H. N. W. Lekkerkerker, J. Phys. Chem. B **105**, 1696 (2001).
[32] D. van der Beek, T. Schilling, and H. N. W. Lekkerkerker, J. Chem. Phys. **121**, 5423 (2004).
[33] D. van der Beek, A. V. Petukhov, S. M. Oversteegen, G. J. Vroege, and H. N. W. Lekkerkerker, Eur. Phys. J. E **16**, 253 (2005).
[34] S. D. Zhang, P. A. Reynolds, and J. S. van Duijneveldt, J. Chem. Phys. **117**, 9947 (2002).
[35] S. D. Zhang, P. A. Reynolds, and J. S. van Duijneveldt, Mol. Phys. **100**, 3041 (2002).
[36] D. van der Beek, H. Reich, P. van der Schoot, M. Dijkstra, T. Schilling, R. Vink, M. Schmidt, R. van Roij, and H. N. W. Lekkerkerker, Phys. Rev. Lett. **97**, 087801 (2006).
[37] A. Chrzanowska, P. I. C. Teixeira, H. Ehrentraut, and D. J. Cleaver, J. Phys.: Condens. Matter **13**, 4715 (2001).
[38] P. I. C. Teixeira, Phys. Rev. E **55**, 2876 (1997).
[39] D. J. Cleaver and P. I. C. Teixeira, Chem. Phys. Lett. **338**, 1 (2001).
[40] P. I. C. Teixeira, A. Chrzanowska, G. D. Wall, and D. J. Cleaver, Mol. Phys. **99**, 889 (2001).
[41] P. I. C. Teixeira, F. Barmes, and D. J. Cleaver, J. Phys.: Condens. Matter **16**, S1969 (2004).
[42] R. Evans, Adv. Phys. **28**, 143 (1979).

[43] L. Onsager, Ann. N.Y. Acad. Sci. **51**, 627 (1949).
[44] J. M. Brader, A. Esztermann, and M. Schmidt, Phys. Rev. E **66**, 031401 (2002).
[45] A. Esztermann, H. Reich, and M. Schmidt, Phys. Rev. E **73**, 011409 (2006).
[46] H. Reich, M. Dijkstra, R. van Roij, and M. Schmidt, J. Phys. Chem. B **111**, 7825 (2007).
[47] H. Reich and M. Schmidt, J. Phys.: Condens. Matter **19**, 326103 (2007).
[48] L. Verlet, Mol. Phys. **41**, 183 (1980).
[49] D. Henderson, K. Y. Chan, and L. Degrève, J. Chem. Phys. **101**, 6975 (1994).
[50] D. Henderson, A. Malijevský, S. Labík, and K. Y. Chan, Mol. Phys. **87**, 273 (1996).
[51] L. Blum and A. J. Torruella, J. Chem. Phys. **56**, 303 (1972).
[52] J. Talbot, A. Perera, and G. N. Patey, Mol. Phys. **70**, 285 (1990).
[53] M. Pernice and H. F. Walker, SIAM J. Sci. Comput. (USA) **19**, 302 (1998).
[54] F. H. Ree and W. G. Hoover, J. Chem. Phys. **40**, 939 (1964).
[55] F. H. Ree and W. G. Hoover, J. Chem. Phys. **46**, 4181 (1967).
[56] W. B. Streett and D. J. Tildesley, Proc. R. Soc. London, Ser. A **348**, 485 (1976).
[57] G. M. Torrie and G. N. Patey, Mol. Phys. **34**, 1623 (1977).
[58] F. G. Wang and D. P. Landau, Phys. Rev. Lett. **86**, 2050 (2001).
[59] F. G. Wang and D. P. Landau, Phys. Rev. E **64**, 056101 (2001).
[60] J. R. Henderson, Mol. Phys. **50**, 741 (1983).
[61] M. P. Allen and D. J. Tildesley, *Computer Simulation of Liquids* (Clarendon Press, Oxford, 1987).
[62] W. H. Press, B. P. Flannery, S. A. Teukolsky, and W. T. Vetterling, *Numerical Recipes in Fortran*, 2nd ed. (Cambridge University Press, Cambridge, England, 1992).
[63] Y. Rosenfeld, Phys. Rev. Lett. **63**, 980 (1989).
[64] Y. Rosenfeld, M. Schmidt, H. Löwen, and P. Tarazona, Phys. Rev. E **55**, 4245 (1997).
[65] Y. Rosenfeld, Phys. Rev. E **50**, R3318 (1994).
[66] Y. Rosenfeld, Mol. Phys. **86**, 637 (1995).
[67] G. Cinacchi and F. Schmid, J. Phys.: Condens. Matter **14**, 12223 (2002).
[68] H. Hansen-Goos and K. R. Mecke (unpublished).
[69] J. Herzfeld, A. Berger, and J. Wingate, Macromolecules **17**, 1718 (1984).
[70] R. van Roij, Eur. Phys. J. E **26**, S57 (2005).
[71] R. F. Kayser and H. J. Raveché, Phys. Rev. A **17**, 2067 (1978).
[72] B. Mulder, Phys. Rev. A **39**, 360 (1989).
[73] J. Stecki and A. Kloczkowski, J. Phys. (Paris) **40**, 360 (1979).
[74] J. Stecki and A. Kloczkowski, Mol. Phys. **42**, 51 (1981).
[75] D.-M. Duh and A. D. J. Haymet, J. Chem. Phys. **97**, 7716 (1992).
[76] R. Evans, J. R. Henderson, D. C. Hoyle, A. O. Parry, and Z. A. Sabeur, Mol. Phys. **80**, 755 (1993).
[77] R. Evans, R. de Carvalho, J. Henderson, and D. Hoyle, J. Chem. Phys. **100**, 591 (1994).
[78] S. V. Savenko and M. Dijkstra, Phys. Rev. E **72**, 021202 (2005).